



# Image-based mesh generation of tubular geometries under circular motion in refractive environments

László Kudela<sup>1</sup> · Felix Frischmann<sup>1</sup> · Ofry E. Yossef<sup>2</sup> · Stefan Kollmannsberger<sup>1</sup> · Zohar Yosibash<sup>3</sup> · Ernst Rank<sup>1,4</sup>

Received: 30 March 2017 / Revised: 14 March 2018 / Accepted: 18 March 2018 / Published online: 20 April 2018  
© Springer-Verlag GmbH Germany, part of Springer Nature 2018

## Abstract

This paper presents an image-based method aimed at generating a mesh of high-order finite elements on a tubular structure. The method assumes that the object is immersed in a liquid with known refractive coefficients and the images are recorded by moving the camera on a circular path around the object. Both the refractive effects and the camera motion are taken into account by a modified bundle adjustment formulation, which allows for an accurate reconstruction even in the presence of the optical interface. A parametric surface is fitted onto the resulting point cloud by an iterative surface fitting algorithm. Finally, the resulting surface is discretized into a mesh of high-order hexahedral elements.

**Keywords** Image-based reconstruction · Mesh generation · Surface fitting · Refractive reconstruction

## 1 Introduction

The reconstruction of three-dimensional objects from images is a widely applied approach in many engineering fields. The main goal of these techniques is to transform the pixel data that are available in the images into a (potentially application-dependent) three-dimensional representation. Depending on the target discipline, such representations can be simple point clouds, triangular meshes, or CAD data formats, such as constructive solid geometry and boundary representation models. Apart from these standard applications, there has been an increasing interest toward methods that provide three-dimensional geometric representations suitable for numerical analysis by means of the finite element method (FEM) and its derivatives [1].

This paper presents a method to create an analysis-suitable high-order finite element mesh, based on a sequence of

images of an object immersed in a liquid with known refractive coefficient. The presented method assumes that the object is tubular—meaning that it can be modeled as a cylinder-like shell—and the camera moves along a circular path around the object, similar to a turntable-like configuration.

One application area of the method is to be seen in experimental studies of the mechanical behavior of soft human tissues in an *in vitro* environment. In these experiments, it is important to be able to mimic the conditions that are present in the normal biological context of the investigated tissues. This usually requires the sample to be immersed in a physiological fluid. An example with such requirements is the study of the active biomechanical response of human arteries. These measurements are challenging for traditional image-based reconstruction methods, because the assumption that light rays propagate along a straight path becomes invalid. Thus, the presence of the interface between the physiological fluid and the camera needs to be taken into account by the reconstruction algorithm.

Photogrammetric measurements in the presence of refractive interfaces have been the subject of extensive research in recent years. In the context of underwater photogrammetry, where the camera is immersed in a liquid medium, the main question is how to account for the distortion effects due to the camera housing [2,3]. Other applications aim at the reconstruction of the refractive interface itself, e.g.,

✉ László Kudela  
laszlo.kudela@tum.de

<sup>1</sup> Chair for Computation in Engineering, Technische Universität München, Arcisstr. 21, 80333 Munich, Germany

<sup>2</sup> Department of Mechanical Engineering, Ben-Gurion University of the Negev, 84105 Beersheba, Israel

<sup>3</sup> School of Mechanical Engineering, Tel-Aviv University, 69978 Ramat-Aviv, Israel

<sup>4</sup> Institute for Advanced Study, Technische Universität München, Munich, Germany

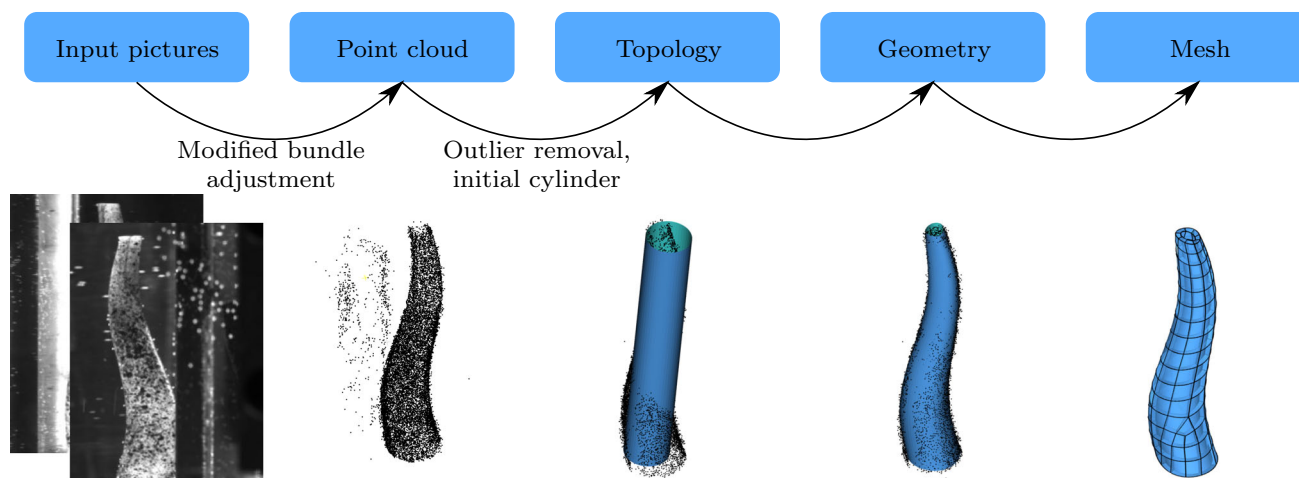


**Fig. 1** Main steps of the proposed approach. The image data are successively transformed into an analysis-suitable finite element mesh

when measuring the shape of transparent or reflective surfaces [4,5].

The goal of generating a high-order finite element mesh is motivated by the superior approximation properties of the high-order finite element method (p-FEM) compared to standard finite elements. Instead of linear shape functions, p-FEM employs high-order polynomials to approximate the solution of physical problems described by partial differential equations [6]. Especially for smooth problems, p-FEM delivers very accurate results with drastically less degrees of freedom compared to linear FEM. The advantages of p-FEM can be fully exploited if it is combined with a high-order discretization of surfaces and volumes.

The method proposed in this paper can be characterized as a multi-stage approach which progressively transforms the pixel data available in the images toward an analysis-suitable finite element mesh. The main steps of the approach are depicted in Fig. 1. In the following, a short overview of each step is given.

The method starts from an image sequence recorded by moving the camera along a circular path around a fixed axis with a constant radius. Assuming that the intrinsic parameters of the camera are known and a rough initial estimate is available for the camera extrinsics, the first step processes the images by a modified bundle adjustment algorithm that provides a 3D point cloud representation of the object. The modified bundle adjustment algorithm—which is the main contribution of this paper—differs in two key aspects from the one used in conventional structure from motion (SfM) applications. Firstly, it incorporates the constraint on the cylindrical movement of the camera, similar to the approach described in [7]. Secondly, it accounts for the refraction effects which are present along the interface between the camera and the object, by utilizing the alternating forward ray tracing (AFRT) algorithm from [8,9].

The aim of the second step is to separate the points in the cloud that belong to the model from those that do not, and to provide an initial estimate on the geometry for subsequent steps. This step is based on the assumption that the shape of the object is tubular, and thus, it can be roughly approximated by a cylinder. This assumption is combined with the random sample consensus algorithm (RANSAC), which removes outliers from the cloud and yields a best-fit cylinder on the remaining points at the same time.

The third step performs surface fitting onto the points in the cloud, using the result of the RANSAC algorithm from the second step as an initial guess. To this end, the best-fit cylinder provided by RANSAC is first converted into a parametric representation. Then, this parametric surface is iteratively deformed toward the inlier points in the cloud, using the active surface algorithm presented in [10].

In the fourth and final step of the procedure a mesh of high-order hexahedral finite elements is generated, using the algorithm of [11], which is especially suited to generate hexahedral meshes on shell-like structures.

The individual steps of the algorithm are discussed in detail in Sect. 2. Section 3 demonstrates the reconstruction pipeline through examples with artificially generated images as well as pictures acquired in laboratory settings. Finally, the paper is summarized in Sect. 4.

## 2 Multi-step reconstruction pipeline

Let  $\mathcal{M}$  denote the object of interest immersed in a liquid with known optical properties. By moving a projective camera around the object along a circular path, a set of images  $\{I_i\}$ ,  $i = 0 \dots n$  is recorded (see Fig. 2). The aim of the reconstruction procedure is to generate a finite element mesh of  $\mathcal{M}$ , starting from the pixel data available in  $\{I_i\}$ . To this

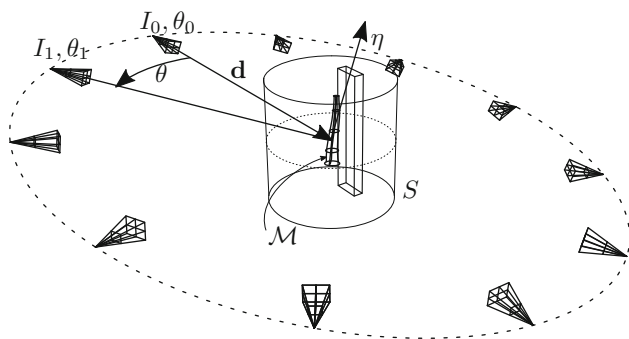


**Fig. 2** Geometric setup of the reconstruction problem. The camera moves around the object of interest  $\mathcal{M}$  along a prescribed circular path. The rectangular box in the vicinity of the object represents objects that do not belong to  $\mathcal{M}$  and may interfere with the reconstruction

end, the images are processed through a multi-step procedure, which is discussed in more detail in the following sections.

### 2.1 Modified bundle adjustment

Following the rules of projective geometry and first assuming that light rays propagate along a straight path, the projection of a feature point  $\mathbf{X}_j$  of  $\mathcal{M}$  onto the  $i$ th image plane is determined by [12]:

$$\mathbf{x}_i^j = \mathbf{K} [\mathbf{R}_i | \mathbf{t}_i] \mathbf{X}_j, \tag{1}$$

where  $\mathbf{K}$ ,  $\mathbf{R}_i$  and  $\mathbf{t}_i$  denote the intrinsics, the rotation and the translation components of the  $i$ th camera, respectively. Equation 1 assumes that the intrinsic parameters of the camera remain unchanged throughout the procedure of acquiring the images, which is why  $\mathbf{K}$  is shared across all the images. If an initial estimate of the camera extrinsics  $\mathbf{R}_i$ ,  $\mathbf{t}_i$  and feature points  $\mathbf{X}_j$  is available, the standard approach to obtain an accurate reconstruction is to solve the following nonlinear least squares problem, also known as *bundle adjustment* [13]:

$$\min_{\mathbf{x}_j, \mathbf{K}, \mathbf{R}_i, \mathbf{t}_i} \sum_i \sum_j (\tilde{\mathbf{x}}_i^j - \mathbf{K} [\mathbf{R}_i | \mathbf{t}_i] \mathbf{X}_j)^2, \tag{2}$$

where  $\tilde{\mathbf{x}}_i^j$  denotes the observed position of  $\mathbf{X}_j$  on the  $i$ th image. The solution of 2 minimizes the sum of the squares of the reprojection errors on all images, for all feature points. In the standard case,  $\mathbf{R}_i$  and  $\mathbf{t}_i$  contribute 6 degrees of freedom to the problem, leading to a total of  $6n$  design parameters associated with the camera extrinsics. However, the constraint on the movement of the camera allows to cast the extrinsic parameters into a more convenient form with less degrees of freedom, following the idea in [7].

Here, each camera is associated with a unique rotation angle  $\theta_i$  around a common rotation axis, defined by a vector  $\eta$  and a translation vector  $\mathbf{d}$ . The rotation axis  $\eta$  is represented in spherical coordinates:

$$\eta = [\sin(\alpha) \cos(\beta), \sin(\alpha) \sin(\beta), \cos(\alpha)],$$

$$\alpha \in [0, \pi], \beta \in [0, 2\pi].$$

This way, there are 5 degrees of freedom associated with the circular path and a single degree of freedom assigned to each camera. Thus, the entire motion of the camera can be described by a total of  $5 + n$  unknowns  $\mathbf{M} = \{\mathbf{d}, \alpha, \beta, \theta_0, \dots, \theta_n\}$ .

The second key ingredient of the bundle adjustment formulation presented herein is a modification of Eq. 1 which accounts for the distortion effects due to the liquid–gas interface. If a light ray with the direction vector  $\mathbf{r}_0$  intersects an optical interface with an outward facing unit normal vector  $\mathbf{n}$ , the direction of the refracted ray  $\mathbf{r}_1$  is determined by the vectorial form of the law of refraction [14]:

$$\mathbf{r}_1 = n_{01} \mathbf{r}_0 + \left[ -n_{01} \mathbf{n} \cdot \mathbf{r}_0 - \sqrt{1 - n_{01}^2 [1 - (\mathbf{n} \cdot \mathbf{r}_0)^2]} \right] \mathbf{n}, \tag{3}$$

where  $n_{01} = n_0/n_1$  is the ratio of the refractive indices of the incident and transmitted media. To account for the refractive effects, the projection of a feature point  $\mathbf{X}_j$  onto the  $i$ th image plane is found using the modified alternating forward ray tracing (AFRT) procedure [8,9]. The basic concepts of AFRT are outlined in the following, complemented by Fig. 3.

Consider a scene with a refractive interface  $S$  and a feature point  $\mathbf{X}_j$  to be projected onto a camera with the projection center  $\mathbf{X}_C$ . The AFRT procedure starts with an initial ray which is determined by connecting  $\mathbf{X}_C$  and  $\mathbf{X}_j$ :

$$\mathbf{r}_0^k = \frac{\mathbf{X}_j - \mathbf{X}_C}{\|\mathbf{X}_j - \mathbf{X}_C\|}, \tag{4}$$

with  $k = 1$  in the first iteration. Evaluating Eq. 3 at the intersection point between the initial ray and the interface  $\mathbf{X}_S^k = \mathbf{r}_0^k \cap S$  yields the direction of the refracted ray  $\mathbf{r}_1^k$ . Next, a ray with direction  $-\mathbf{r}_1^k$  is traced from  $\mathbf{X}_j$  toward the interface  $S$ . This gives a new intersection point  $\mathbf{X}_S^k$ . If the distance  $\Delta \mathbf{X}_k = \|\mathbf{X}_S^k - \mathbf{X}_S^{k-1}\|$  is larger than a tolerance value  $\epsilon$ , the procedure is reiterated with:

$$\mathbf{r}_0^{k+1} = \frac{\mathbf{X}_S^{k+1} - \mathbf{X}_C}{\|\mathbf{X}_S^{k+1} - \mathbf{X}_C\|}, \tag{5}$$

where  $\mathbf{X}_S^{k+1}$  is defined by the projection of  $\frac{1}{2} (\mathbf{X}_S^k + \mathbf{X}_S^{k-1})$  onto  $S$ . The iteration terminates when  $\Delta \mathbf{X}_k < \epsilon$ . Finally, the projection of  $\mathbf{X}_S^{k_{end}}$  onto the image plane by Eq. 1 yields  $\mathbf{x}_i^j$ .

We denote the projective action of the AFRT procedure on the feature point  $\mathbf{X}_j$  for the  $i$ th image by:

$$\mathbf{x}_i^j = P_{AFRT} (\mathbf{X}_j, \mathbf{K}, \eta, \mathbf{d}, \theta_i, \sigma), \tag{6}$$

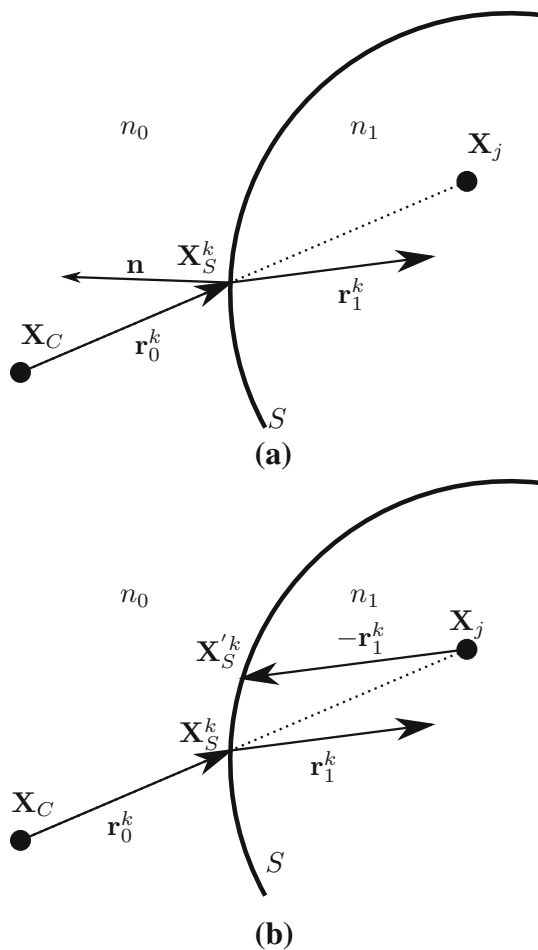


**Fig. 3** Schematic of the AFRT algorithm. **a** The refracted direction  $\mathbf{r}_1^k$  is computed at  $\mathbf{X}_S^k$ . **b** The ray  $-\mathbf{r}_1^k$  is traced toward  $S$ , resulting in  $\mathbf{X}_S'^k$

where the vector  $\sigma$  represents the set of parameters that describes the geometry of the interface. If, for example, the shape of the interface is cylindrical,  $\sigma$  contains its orientation, location, radius and the corresponding refractive coefficients.

By taking the constraint of circular motion and the effects of the refractive imaging process into account, the bundle adjustment problem can be restated in the following form:

$$\min_{\mathbf{X}_j, \eta, \mathbf{d}, \mathbf{K}, \theta_i, \sigma} \sum_i \sum_j \left( \tilde{\mathbf{x}}_i^j - P_{\text{AFRT}}(\mathbf{X}_j, \mathbf{K}, \eta, \mathbf{d}, \theta_i, \sigma) \right)^2. \quad (7)$$

Note that here the projective relationship of Eq. 1 is replaced by the AFRT procedure.

An initial guess regarding the parameters is required in order to solve the bundle adjustment problem. As our proposed algorithm is aimed at 3D reconstruction from images recorded in experimental environments, we assume that the camera is calibrated prior to the experiments; therefore,  $\mathbf{K}$  is known. Further, we assume that estimates of the camera

motion parameters  $(\mathbf{n}, \theta_i)$  and the parameters of the optical interface ( $\sigma$ ) are available, e.g., by manual measurements. This allows to estimate the initial position of the  $\mathbf{X}_j$ 's by identifying corresponding feature locations across all images and by intersecting the (refracted) rays associated with them. Our experience is that the algorithm behaves fairly robust even if there is as much as 10% error in the initial estimate on the position of the rotation axis, as well as the parameters of the cylinder. Concerning the orientation of the rotation axis, we have found that the difference between the initial estimate and the real value should not exceed  $15^\circ$ – $20^\circ$ . Such values are easy to obtain in a laboratory setup. In our practical examples, we use the scale-invariant feature transform (SIFT) [15] to detect and describe features on the input images. The matching of features across images is performed by approximate nearest neighbor search. We use the implementation of both algorithms from the open source multi-view geometry library OpenMVG [16].

## 2.2 Outlier removal, initial estimation of the geometry

Solving the bundle adjustment problem in Eq. 7 yields a set of points  $\{\mathbf{X}_j\}$ . However, some points in this set do not belong to  $\mathcal{M}$ : the sources of these *outlier points* are objects that are part of the experimental apparatus or the environment. The outlier points are removed by applying the random sample consensus (RANSAC) procedure [17] on the set  $\{\mathbf{X}_j\}$ , which is especially suited to fit mathematical models to scattered data in the presence of outliers. Knowing that  $\mathcal{M}$  is a tubular structure and thus can be approximated by a cylinder, the model to be fitted by RANSAC is a cylinder with a parameter vector  $\pi = \{\mathbf{d}, \mathbf{p}_0, r\}$ , where  $\mathbf{d}, \mathbf{p}_0 \in \mathcal{R}^3$  denote the orientation and the placement of the cylinder axis, while  $r$  represents its radius.

The RANSAC procedure results in a reduced set of points  $\{\mathbf{X}_j^{\mathcal{M}}\}$ , representing the inliers with respect to the shape of interest  $\mathcal{M}$ . Further, the parameter vector  $\pi$  contains information about the placement, orientation and radius of the best-fit cylinder.

## 2.3 Iterative surface fitting

Having removed the outliers and after obtaining a rough estimate regarding the orientation and overall radius of the geometry, this step proceeds by fitting a parametric surface onto  $\{\mathbf{X}_j^{\mathcal{M}}\}$ . For this purpose, the approximate cylinder of the previous step is converted to a B-Spline surface representation of the form:

$$\mathbf{S}(u, v) = \sum_{i=1}^n B_i(u, v) \mathbf{P}_i, \quad (8)$$

where each  $B_i(u, v)$  represents a bivariate piecewise polynomial basis function with an associated control point  $\mathbf{P}_i$ . Starting from the initial guess, the surface fitting follows the procedure described in [10]. Here, only the basic concepts of the algorithm are summarized. Figure 4 provides an overview of the main steps in 2D.

The main idea of the procedure is to iteratively deform the surface  $\mathbf{S}(u, v)$  toward the model points  $\{\mathbf{X}_j^M\}$ , with the help of local quadratic approximants of the squared distance function. To this end, a set of *active surface points*  $\{\mathbf{s}_k\}, k = 1 \dots M$  is generated by evaluating  $\mathbf{S}(u, v)$  on a regular grid of parameter locations  $\{(u_k, v_k)\}$ . Then, for each  $\mathbf{s}_k$ , the closest point  $\mathbf{p}_k$  is found in the set  $\{\mathbf{X}_j^M\}$  together with its  $k$  nearest neighbors. This allows to estimate the local principal curvatures  $\kappa_1$  and  $\kappa_2$  of the point set at  $\mathbf{p}_k$ , using the method of osculating jets—as presented in [18].

Using the curvature estimates, a local quadratic approximate of the squared distance function can be computed at each  $\mathbf{s}_k$ , following [19]:

$$F_d^k(x_1, x_2, x_3) = \frac{d}{d - \rho_1}x_1^2 + \frac{d}{d - \rho_2}x_2^2 + x_3^2, \tag{9}$$

where  $d$  denotes the distance between  $\mathbf{s}_k$  and  $\mathbf{p}_k$ ,  $\rho_i = 1/\kappa_i$ , and  $x_i$ 's denote the coordinates in the local principal frame at  $\mathbf{p}_k$ .

The surface fitting problem amounts to finding a displacement vector  $\mathbf{c}_i$  for each control point  $\mathbf{P}_i$  that minimizes:

$$F = \sum_{k=1}^M F_d^k \left( \sum_{i=1}^n B_i(u_k, v_k) (\mathbf{P}_i + \mathbf{c}_i) \right). \tag{10}$$

It was shown in [10] that minimizing  $F$  amounts to solving a system of linear equations:

$$2\mathbf{A}\mathbf{c} + \mathbf{b} = 0, \tag{11}$$

where the vector  $\mathbf{c}$  (of size  $3n \times 1$ ) collects the displacement vectors of the control points:  $\mathbf{c} = [\mathbf{c}_1, \mathbf{c}_2, \dots, \mathbf{c}_n]^T$ . The next iteration starts with an updated surface whose control points are shifted by the values in  $\mathbf{c}$ , and the procedure is repeated until the root-mean-squared approximation error is less than a tolerance value.

### 2.4 Generation of a high-order finite element mesh

The final step of the reconstruction procedure generates a high-order hexahedral finite element mesh. To this end, the mesh generation algorithm from [11] is employed. This procedure aims at generating volumetric meshes on shell-like structures by enhanced sweeping methods. In the first step of this procedure, the B-Spline surface of the previous step is

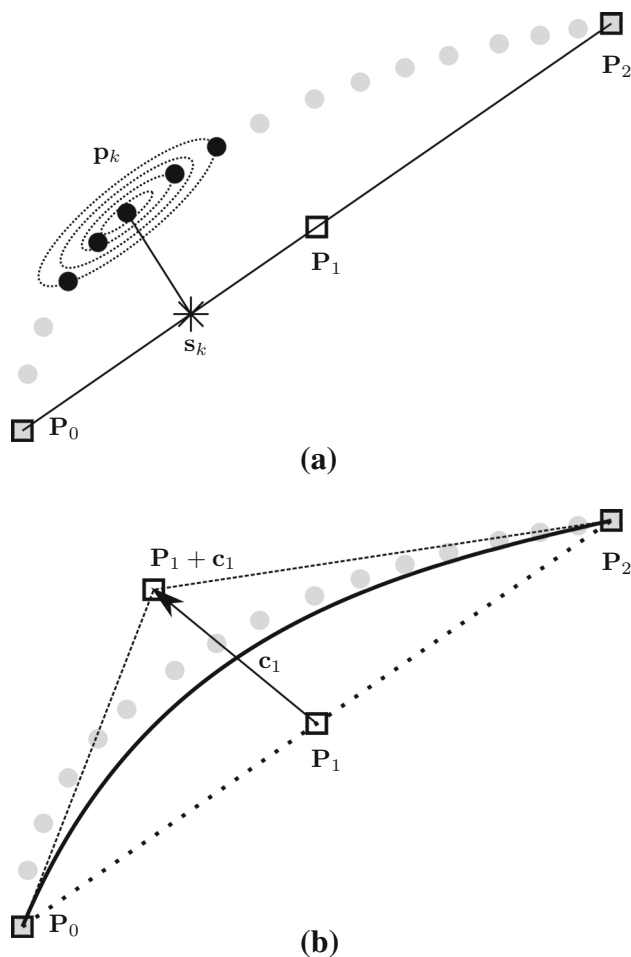


**Fig. 4** Conceptual sketch of the active surface fitting algorithm in 2D. The gray dots represent the point cloud  $\mathbf{X}_j^M$ , while the solid black curve depicts the active curve which is iteratively deformed toward  $\mathbf{X}_j^M$ . **a** For an active point  $\mathbf{s}_k$ , the approximant of the squared distance function is computed by finding  $\mathbf{p}_k$  and its  $k$ -neighborhood. **b** After solving Eq. 11, the control point  $\mathbf{P}_1$  is shifted by the vector  $\mathbf{c}_1$

discretized into high-order quadrilateral elements. The mapping functions of these elements are defined by Lagrangian polynomials combined with a set of interpolation points distributed on  $\mathbf{S}_{\mathcal{M}}(u, v)$ . Then, these elements are swept in the direction of the local surface normals, providing a mesh of hexahedral elements. To determine the sweeping distance of this step, the local thickness of the geometric model has to be specified at each interpolation point of the surface. For the sake of simplicity, the thickness values in our examples are defined as constant.

## 3 Examples

This section demonstrates the reconstruction algorithm on artificially generated images as well as on pictures recorded in real-world scenarios.

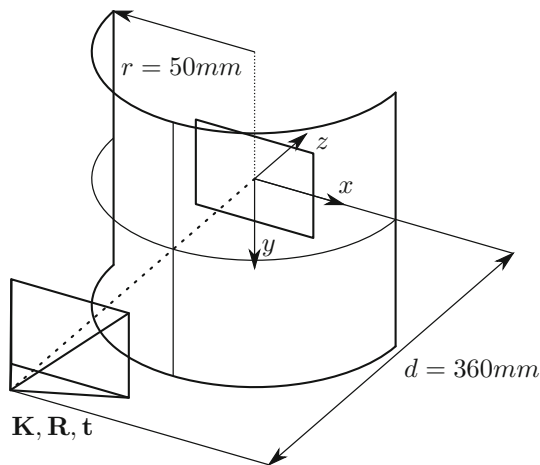


**Fig. 5** Setup of the test example with a single camera and a checkerboard pattern immersed in a cylindrical water container

### 3.1 Effects of refraction

Before demonstrating the entire mesh generation procedure, the importance of including the refractive effects in the bundle adjustment formulation is demonstrated. To this end, we consider a scenario where a planar object of size  $25 \text{ mm} \times 19 \text{ mm}$  with a checkerboard pattern is immersed in a cylindrical container filled with water. The image of the checkerboard is recorded on a single camera using ray tracer software. The imaging setup is depicted in Fig. 5. The positions of the individual checkerboard corners on the synthetically generated images are detected using the checkerboard detector algorithm of OpenCV [20]. Let  $\mathbf{X}_j^G$  denote the coordinates of checkerboard corners in world coordinates,  $\tilde{\mathbf{x}}_j$  the image coordinates of the detected corners,  $\mathbf{x}_j^P$  and  $\mathbf{x}_j^{\text{AFRT}}$  the projection of the checkerboard corners onto the image plane of the camera using standard perspective projection and the algorithm, respectively. The norm of the reprojection error for an individual corner with perspective projection can be defined as:

$$e_j = \left\| \tilde{\mathbf{x}}_j - \mathbf{x}_j^P \right\|_2. \quad (12)$$

The reprojection error of the AFRT algorithm can be computed similarly. Figure 6 shows the error of the standard perspective projection in the image coordinate space. In this imaging configuration, the light rays associated with the pixels around the image center enter the refractive medium almost orthogonally, which means that they are not subject to significant refraction and their direction remains almost unchanged. Therefore, the error associated with the pixels around the center of the image is low, as also shown in the figure. For image points that are further away from the imaging center, however, the refractive effects dominate the error. Compared to the values obtained by the AFRT algorithm,

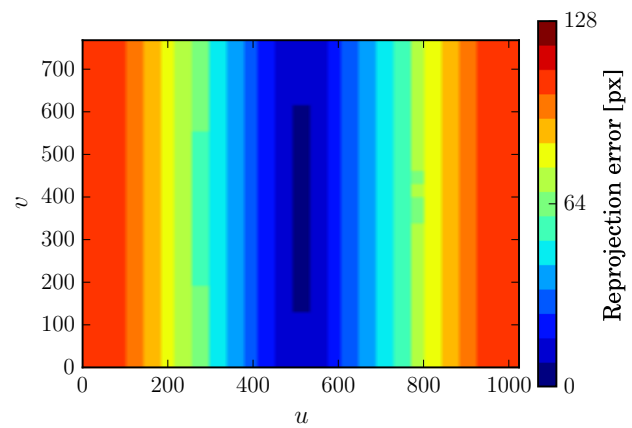


**Fig. 6** Reprojection errors due to refractive effects for the checkerboard example. The error is small around the camera center and increases toward the image boundaries

which remain in the sub-pixel accuracy range, this error can be orders of magnitudes higher.

This example emphasizes that if the refractive effects are not accounted for, the value of the objective function in the bundle adjustment problem (Eq. 2) remains high—even if the exact values of the structure points  $\mathbf{X}_j^G$  and the camera parameters  $\mathbf{K}$ ,  $\mathbf{R}_i$ ,  $\mathbf{t}_i$  are substituted into the equation. Moreover, the minimum of the objective function does not occur at these set of parameters at all. Instead, the nonlinear least squares solver that is used to solve the bundle adjustment problem is drawn to a minimum, which is physically wrong.

To demonstrate this effect, we consider a simplified bundle adjustment problem of the imaging setup of Fig. 5. In this case, the camera is allowed to move only along the  $z$ -axis, while all the other parameters—including the structure points—are fixed. For different distance values  $d$ , the root-mean-squared (RMS) error of the reprojection is computed as:

$$e_{\text{RMS}}^P = \sqrt{\frac{1}{n} \sum_j (\tilde{\mathbf{x}}_j - \mathbf{x}_j^P)^2}, \quad (13)$$

where  $n$  denotes the number of checkerboard corners. The root-mean-squared error for the AFRT projection can be computed similarly. Figure 7 shows the RMS error for different distance values. As expected, when using the AFRT algorithm, the minimum of the RMS error occurs when  $d$  is equal to the camera distance used in the ray tracing software. In contrast, the standard perspective projection attains its minimum at a different distance value  $d$ , which does not correspond to the real location of the camera.

A similar effect can be observed if the camera parameters are kept fixed and the structure points  $\mathbf{X}_j$  are allowed to move. To this end, the setup of Fig. 5 is extended by two additional cameras, as depicted in Fig. 8. If the AFRT algorithm in the

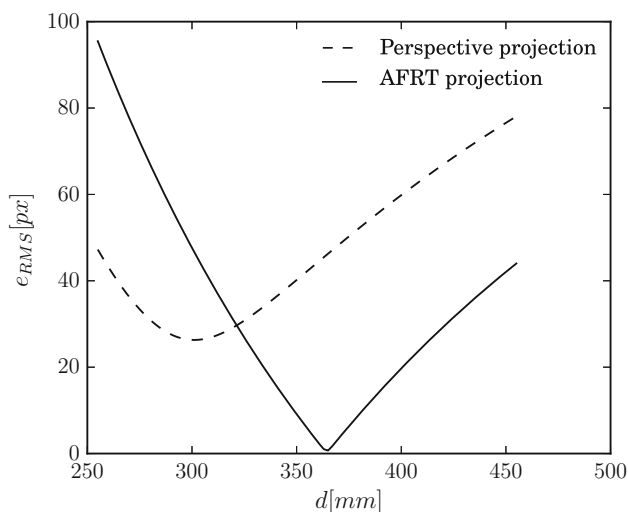


**Fig. 7** Root-mean-squared reprojection error for different camera distances for the checkerboard example. With standard perspective projection, the minimum occurs at the incorrect distance  $d = 300$  mm. The AFRT algorithm delivers a well-defined minimum at  $d = 360$  mm, which corresponds to the reference configuration

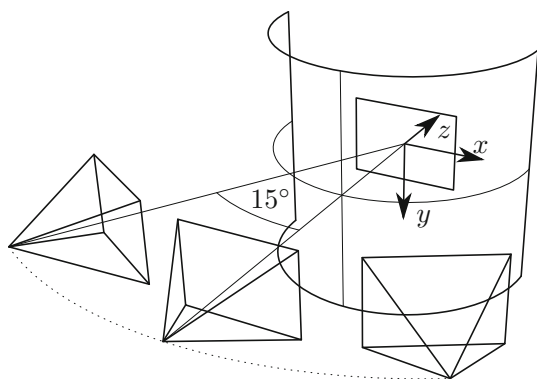


**Fig. 8** Multi-camera setup of the checkerboard test example

bundle adjustment problem, the resulting minimizer set of structure points matches the reference points  $\mathbf{X}_j^G$  with high accuracy. In contrast, if the refractive effects are disregarded, the structure points differ significantly from the reference configuration, as depicted in Fig. 9. Table 1 summarizes the errors with respect to the ground truth geometry along the main directions of the world coordinate system as well as the root-mean-square of the reprojection error obtained from the solution of the bundle adjustment problem. Note that even though the values of the reprojection errors are in the same order of magnitude, there is a large difference in the error of the structure points.

This implies that neglecting the refraction of light in the bundle adjustment formulation leads to an error both in the estimated structure points as well as in the estimated camera positions.

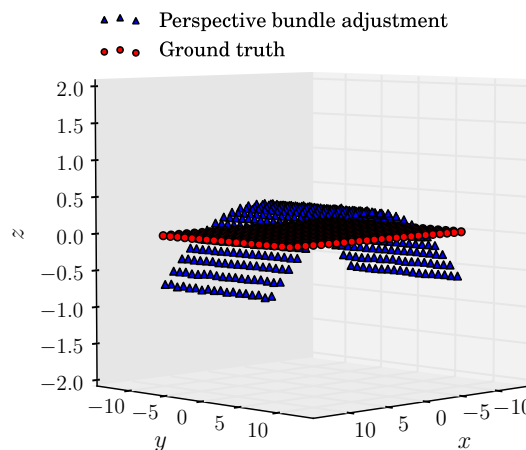


**Fig. 9** Ground truth points and structure points found by bundle adjustment using perspective projection, for the multi-view checkerboard example

Another important aspect that needs to be considered when using the AFRT algorithm is the increase in time needed to solve the bundle adjustment problem. With standard perspective projection, the image of a structure point on the image plane can be computed directly by evaluating Eq. 1. The AFRT procedure, however, requires an evaluation of the ray–surface intersections and the law of refraction across many iterations. Obviously, the higher the refractive effects, the more AFRT iterations are required. For the checkerboard example, this relationship is depicted in Fig. 10. As expected, the rays that are associated with pixels around the image center—where refraction plays a minor role—require less computation. For pixels that are further away from the center, the required number of iterations increases, which directly affects the overall runtime of the bundle adjustment problem. These considerations need to be taken into account when deciding how the object is to be positioned inside the fluid container. Concerning tubular structures, this usually means that the orientation of the structure should be chosen such that it is aligned with the principal axis of the cylindrical container.

### 3.2 Tubular object in synthetic images

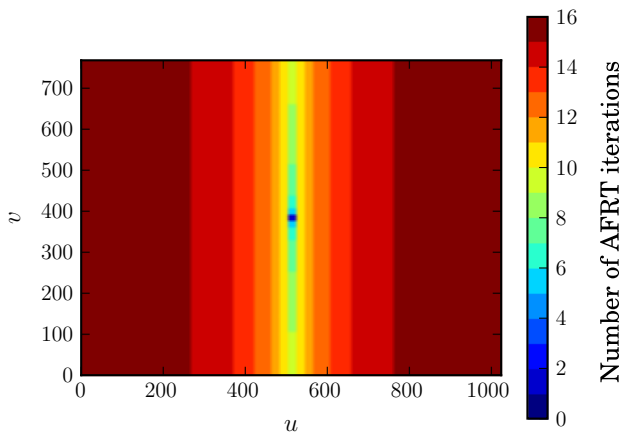
This section demonstrates the reconstruction of a tubular object on a set of pictures obtained from a ray tracer software. In this setup, an object  $\mathcal{M}$  (depicted in Fig. 11) is immersed in a liquid with known optical properties. The geometry was constructed by sweeping a circle along a parametric generator curve defined by:

$$\mathbf{g}(t) = \left[ t, \sin\left(\frac{2\pi}{30}t\right), 0 \right]^T, \quad t \in [0, 30]. \tag{14}$$

**Table 1** Summary of error values for the checkerboard example

Method	$\Delta X_{\text{RMS}}$ (mm)	$\Delta Y_{\text{RMS}}$ (mm)	$\Delta Z_{\text{RMS}}$ (mm)	$\Delta \mathbf{X}_{\text{RMS}}$ (mm)	$e_{\text{RMS}}$ (px)
Perspective projection	0.601	0.8052	0.3193	0.609	0.59
AFRT projection	0.0055	0.0090	0.0052	0.0068	0.84

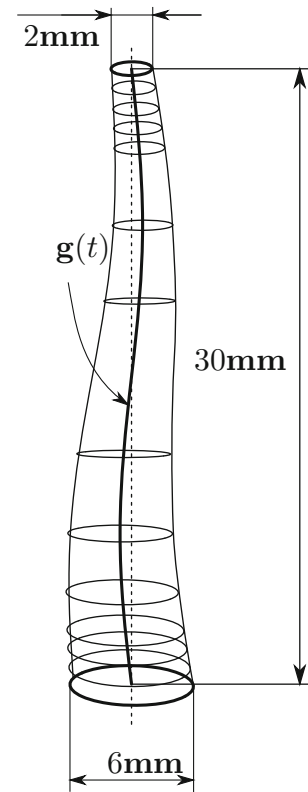
Even though the reprojection error  $e_{\text{RMS}}$  is in the same order of magnitude for both methods, there is a significant difference in the error of the structure points

**Fig. 10** Number of AFRT iterations across the image coordinates for the checkerboard example

In the sweeping process, the radius of the circle is increased linearly along the generator curve, such that  $r(t=0) = 1$  and  $r(t=30) = 3$ . The shape of the refractive interface is cylindrical, with a radius  $R = 50$  mm, and the camera moves along a circular path around the object as shown in Fig. 2. To investigate how the method behaves for various object poses, the reference geometry was placed inside the water container in three different configurations, which are depicted in Fig. 12. In these configurations, the angle between the principal axis of the object and the vertical direction is  $0^\circ$ ,  $45^\circ$  and  $90^\circ$ , respectively. The center and the axis of the camera path were deliberately chosen in such a way that they do not coincide with the location and the axis of the refractive interface, nor with the object. Figure 13 shows examples of the captured images for pose A at different camera positions.

The solution of the bundle adjustment problem of Sect. 2.1 yields a set of parameters that minimize the sum of the squares of the reprojection errors for all feature points over all images. To measure how accurately the bundle adjustment method is able to fit the model parameters to the observations, we look at the root-mean-square of the reprojection errors:

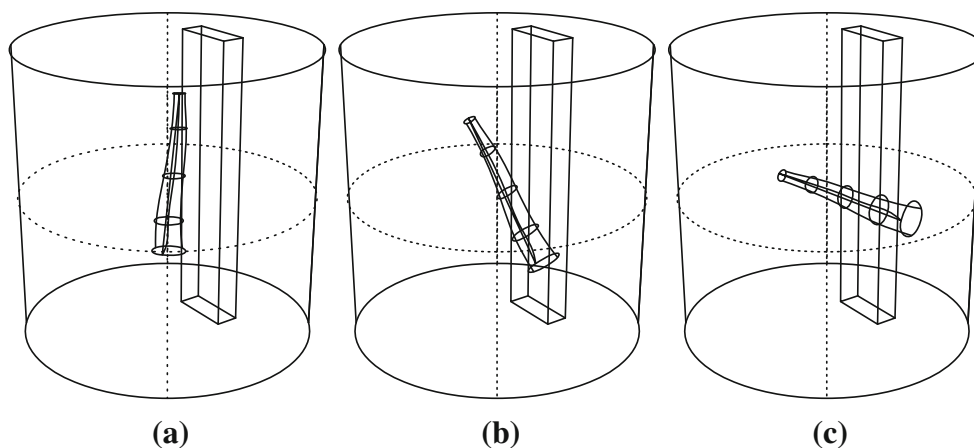
$$e_{\text{RMS}} = \sqrt{\frac{1}{n} \sum_i \sum_j \left( \tilde{\mathbf{x}}_i^j - P_{\text{AFRT}}(\mathbf{X}_j, \mathbf{K}, \mathbf{n}, \mathbf{d}, \theta_i, \sigma) \right)^2}, \quad (15)$$

**Fig. 11** Reference geometry  $\mathcal{M}$  used in the verification example

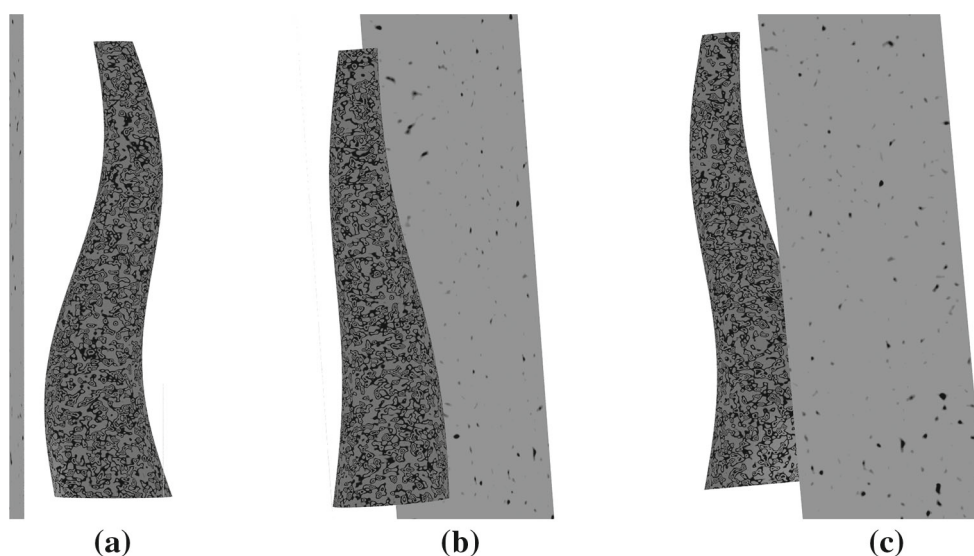
where  $n$  denotes the total number of residuals. Secondly, knowing the geometry of  $\mathcal{M}$  allows to investigate the accuracy of the optimized set of structure points  $\{\mathbf{X}_i\}$ , by computing the signed distance of each  $\mathbf{X}_i$  with respect to the model  $\mathcal{M}$ , denoted by  $d(\mathbf{X}_i, \mathcal{M})$ . To calculate the signed distance, the closest orthogonal projection of every  $\mathbf{X}_i$  onto  $\mathcal{M}$  is computed. This way, the mean signed distance with respect to the ground truth is calculated as:

$$e_{\mathcal{M}} = \frac{1}{N} \sum_i d(\mathbf{X}_i, \mathcal{M}). \quad (16)$$

In order to compare the method to the standard bundle adjustment, the reconstruction of the artificially generated images was also performed without taking the refractive effects into account, and allowing the cameras to move arbitrarily.



**Fig. 12** Different object poses used in the synthetic example. **a** Pose A. **b** Pose B. **c** Pose C



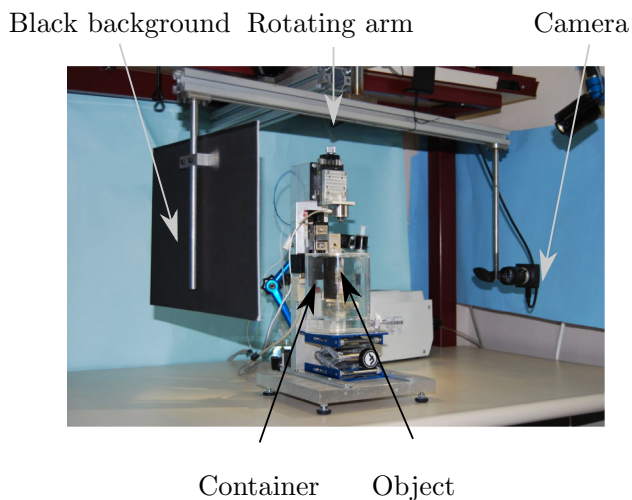
**Fig. 13** Synthetic images of pose A. The object was immersed in water, and the pictures were recorded under different rotations  $\theta$  of the camera. **a**  $\theta = 0^\circ$ . **b**  $\theta = 108^\circ$ . **c**  $\theta = 227^\circ$

Table 2 summarizes the results for the different configurations. Concerning the number of points and the precision of the resulting point cloud, pose A outperforms the two other settings. On the other hand, similarly to pose C, it requires more iterations in the solution process than pose B. The reason for this is that the projection of the object in the first and third configuration only covers a rather narrow region on the captured images as the camera rotates, leaving most of the image area unexploited. As demonstrated by the checkerboard example in Sect. 3.1, the least amount of AFRT iterations is needed if the object is oriented along the principal axis of the water container. In contrast, if the object is oriented perpendicularly—as in the case of pose C—the number of iterations of the AFRT algorithm increases. This also correlates with the average cost of evaluating a single residual.

Similarly to the checkerboard example in Sect. 3.1, when the refractive effects are neglected, the average mean distance of the resulting structure points  $\{\mathbf{X}_i\}$  is rather high, even though the standard bundle adjustment yields a set of parameters that minimize the reprojection errors to a sub-pixel accuracy. This is due to the fact that in the standard case, the standard bundle adjustment finds a set of parameters that minimizes the cost function of Eq. 2, but this optimal set of parameters does not represent the real structure at all. In contrast, the structure points resulting from the modified bundle adjustment approach—which takes the refractive effects into account—are orders of magnitude closer to the ground truth shape  $\mathcal{M}$ , while the reprojection errors are in the same order of magnitude. This high difference in the mean signed distances can be observed both for the synthetically generated images and for those recorded in the real setting, as will be shown in the next section.

**Table 2** Comparison of bundle adjustments for different poses of the verification geometry

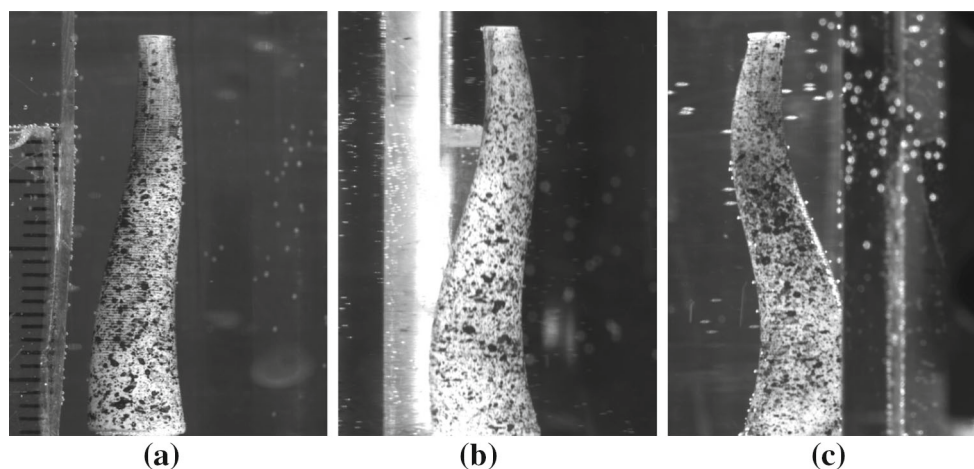
Pose	$e_{RMS}$ (px)	$e_M$ (mm)	# Points	# Residuals	# Iterations	Avg. AFRT iterations	#	Time per residual
<i>Modified bundle adjustment</i>								
A	0.3987	0.0059	14,467	197,428	27	18		$2.56 \times 10^{-5}$ s
B	0.2575	0.026	14,011	148,042	16	21		$2.76 \times 10^{-5}$ s
C	0.306	0.1575	9185	101,672	27	23		$3.42 \times 10^{-5}$ s
<i>Standard bundle adjustment</i>								
A	0.2551	0.8701	14,399	196,276	35	–		$5.72 \times 10^{-7}$ s
B	0.7366	0.6772	13,917	143,854	13	–		$5.73 \times 10^{-7}$ s
C	0.702	0.430603	9185	101,672	13	–		$5.62 \times 10^{-7}$ s

**Fig. 14** Laboratory setup of the verification example. The camera is mounted on an arm that rotates around a cylindrical container. To avoid unwanted background features, a black sheet of light-absorbing material is mounted on an arm opposite to the camera. The 3D printed reference object is placed inside the container

### 3.3 Tubular objects represented on real images

For comparison, the experiment of the previous section was repeated in a real setting. In this case, the geometry was manufactured using a 3D printer and it was immersed into a cylindrical water container, according to pose A from the previous section. To enhance the quality of the surface texture, the model was sprayed with black ink using an air-brush. The resulting dot-like pattern covers approximately 40% of the surface. A camera was moved around the object using an automatic device (Fig. 14), allowing for accurate angular positioning and keeping the radius of the camera's path constant. This automatic device is part of an experimental apparatus built for the purpose of investigating the active biomechanical behavior of human arteries. A detailed description of these experiments and the apparatus can be found in [21].

Prior to the experiment, the intrinsic parameters were calibrated using the method of [22]. With an increment of  $10.8^\circ$  in the angular position of the camera, 22 images of the object were captured. Examples of the images taken in the real set-

**Fig. 15** Images taken of the object immersed in water, under different rotation angles  $\theta$  of the camera. **a**  $\theta = 0^\circ$ . **b**  $\theta = 108^\circ$ . **c**  $\theta = 227^\circ$

**Table 3** Comparison of the results of standard bundle adjustment and its modified version for the real image set

Method	$e_{\text{RMS}}$ (px)	$e_{\mathcal{M}}$ (mm)	# Points
Standard B.A.	0.2551	0.8701	7727
Modified B.A.	0.3987	0.0059	8800

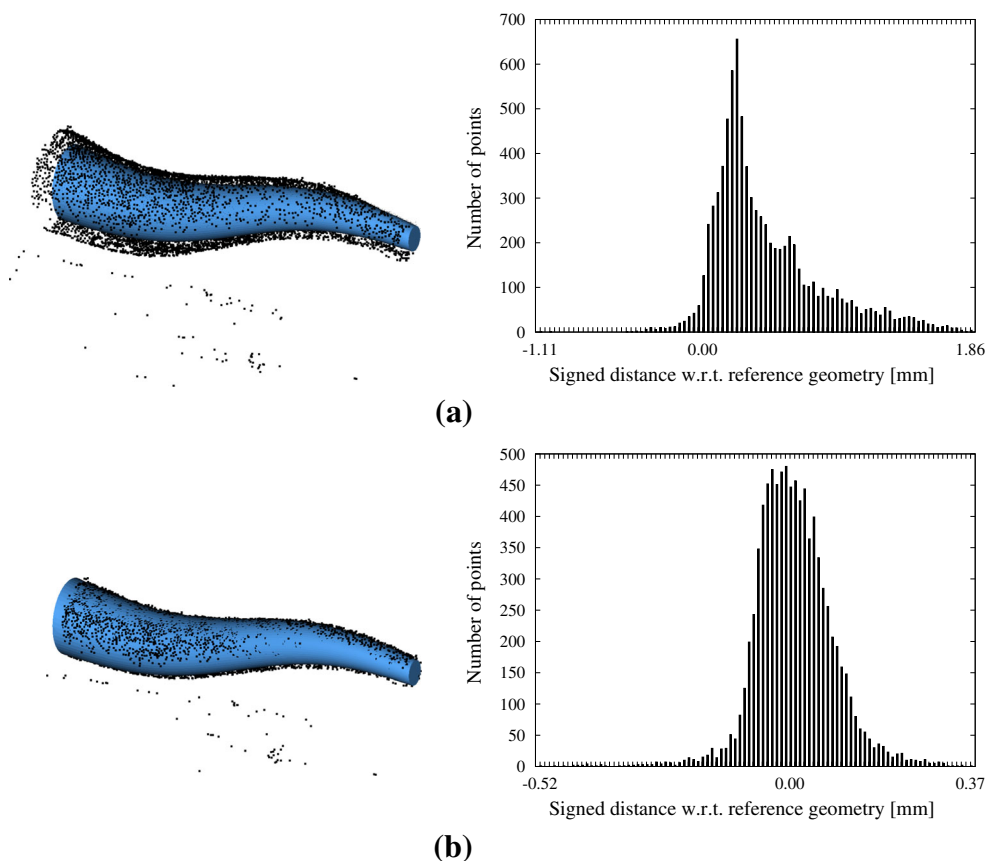
ting are depicted in Fig. 15. The results of the modified bundle adjustment on the real image data are summarized in Table 3. Similar to the examples with the synthetic images, the root-mean-squared of the reprojection error is in the same order of magnitude for both methods. However, the modified bundle adjustment formulation yields points that lie orders of magnitudes closer to the ground truth geometry. The point sets and histograms of the signed distance errors for this scenario are depicted in Fig. 16.

As shown in Fig. 16, the resulting point set also  $\{\mathbf{X}_i\}$  contains points that belong to the experimental environment. These outlier points are filtered out using the RANSAC algorithm, as explained in Sect. 2.2. Apart from the remaining inlier points  $\{\mathbf{X}_i^{\mathcal{M}}\}$ , RANSAC also provides the parameters of the cylinder which is the best fit to these points.

Concerning the points computed by the modified bundle adjustment method, the estimated diameter given by the RANSAC algorithm is 2.47763 mm. This value corresponds to a difference of 1% compared to the average radius of the reference geometry  $\mathcal{M}$ . In contrast, the points resulting from the standard bundle adjustment have a diameter of 3.40295 mm, which means a difference of 40%.

As described in Sect. 2.3, the best-fit cylinder is used as the initial estimate for the active surface fitting algorithm of [10]. Starting from an initial 300 points, the number of active surface points is increased by 100 in every iteration, and the iteration is repeated until the root-mean-squared distance of the active surface with respect to the point cloud falls below 0.01 mm. The resulting surface  $\mathbf{S}_{\mathcal{M}}(u, v)$  is a tensor product B-Spline surface approximating  $\mathcal{M}$ . This surface is stored as a boundary representation model (B-Rep) for the final step. The initial estimate and the result of the surface fitting algorithm are depicted in Fig. 17.

In the final step of the reconstruction procedure, a mesh of curved hexahedral finite elements is created by employing the method of [11]. Figure 18 shows an example mesh with quadratic elements. For this mesh, the average signed dis-

**Fig. 16** Point clouds resulting from the real image set and the respective histograms of signed distance errors. **a** Standard bundle adjustment. **b** Modified bundle adjustment

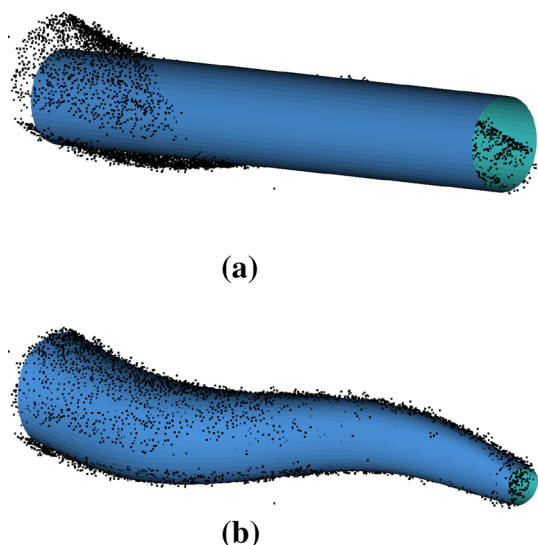


**Fig. 17** Initial estimate and fitted surface. **a** Inlier points and best-fit cylinder. **b** Surface fitted onto the inlier points

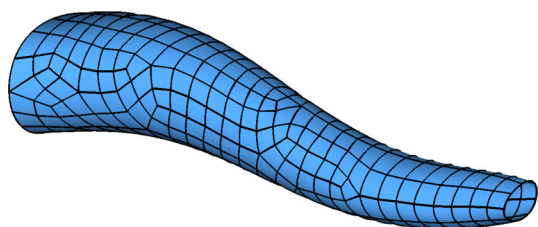


**Fig. 18** Surface mesh: quadratic quadrilateral elements

tance of the interpolation points with respect to the reference geometry  $\mathcal{M}$  is 0.009 mm.

To obtain a volumetric mesh of high-order finite elements, the quadrilateral elements are swept in the direction of the local surface normals of  $\mathbf{S}_{\mathcal{M}}(u, v)$ . In this example, the thickness of the geometry was chosen to be a constant of  $t = 0.5$  mm throughout the entire domain. Examples of quadratic and quartic hexahedral elements are depicted in Fig. 19.

### 3.4 Tubular object with a branch represented on real images

As a final demonstration of the entire mesh generation procedure, we consider a branched geometry—represented by the intersection of two tubular objects, as depicted in Fig. 20. The length of the object is 150 mm, an order of magnitude bigger than in the previous example. The texture of the object was enhanced by spraying black ink on its surface. Similar to the previous example, the object was placed in a cylindrical water container, and 36 pictures were recorded by moving the camera around it along a circular path. As an example, Fig. 21 depicts one of the images captured by the camera.

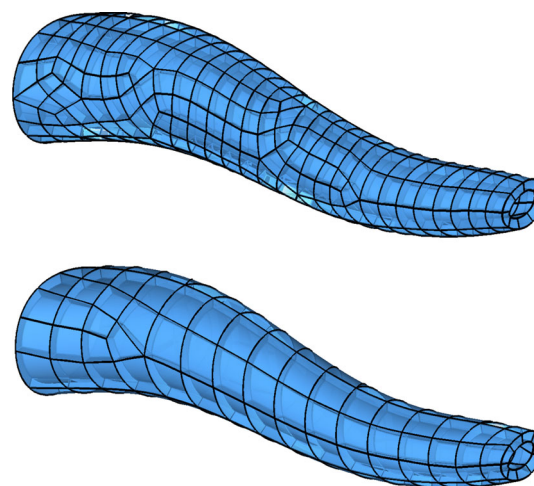


**Fig. 19** Volumetric mesh: quadratic and quartic hexahedra



**Fig. 20** Tubular geometry with a branch

As the first step in the procedure, a point cloud is generated using the modified bundle adjustment formulation. The resulting points are depicted in Fig. 22. The average distance of the resulting 10,626 structure points to the ground truth geometry is 0.19 mm.

After solving the modified bundle adjustment problem, the RANSAC algorithm identifies the two main cylindrical components in the cloud. The points are separated according to the cylindrical model they belong to. The resulting cylinders represent the topology of the object, as shown in Fig. 23 as well.

The two cylinders resulting from the RANSAC algorithm are converted to separate B-Spline surfaces and used as initial guesses for the iterative procedure of Sect. 2.3. This process finds the best-fit surface to the separated points. The resulting surfaces are intersected and joined together to form the final geometric model, which is depicted in Fig. 24.

Finally, a mesh of high-order finite elements is generated on the B-Rep surface using the algorithm of [11]. An example of a mesh consisting of quadratic hexahedral elements is depicted in Fig. 25. The nodes of the resulting mesh lie within 0.25 mm of the ground truth geometry.



**Fig. 21** Image taken of the branched geometry in the experimental system

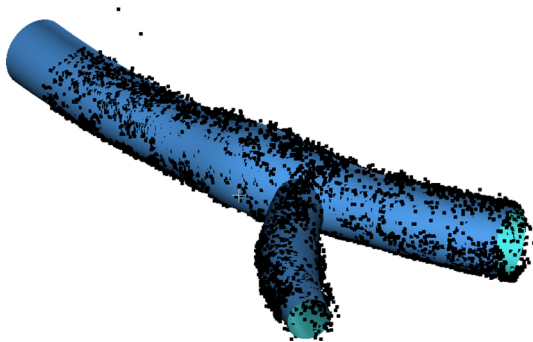


**Fig. 22** Point cloud resulting from bundle adjustment, and the ground truth geometry

## 4 Conclusions

In this paper, we presented an image-based technique that serves to generate a mesh of high-order finite elements on a tubular geometry which is immersed in a liquid with known refractive coefficients. The method uses photographs that were recorded by moving a camera along a circular path around the object. Further, it is assumed that a geometric description of the refractive interface is available. In the first step, the method uses a modified bundle adjustment approach, which differs from the standard technique in two

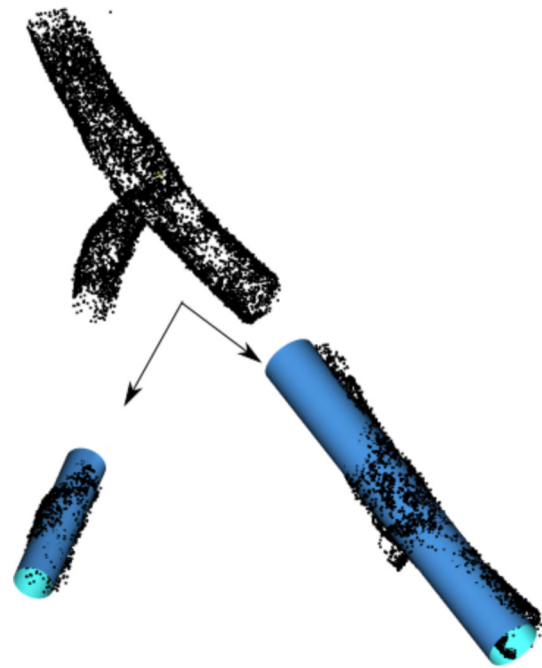


**Fig. 23** The RANSAC algorithm separates the point cloud according to the underlying cylindrical models that describe its topology

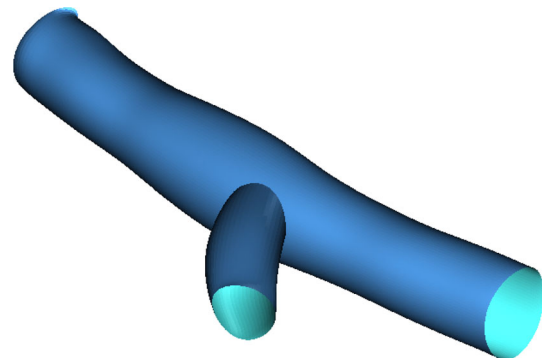


**Fig. 24** B-Spline surfaces fitted onto the points separated by the RANSAC step

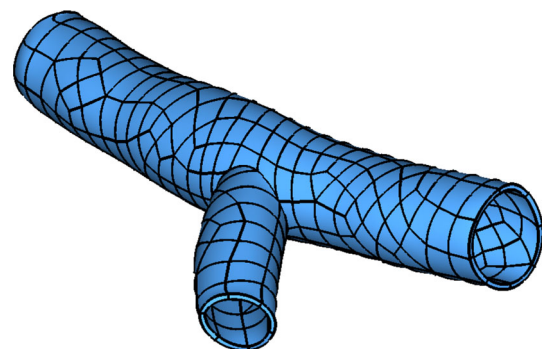


**Fig. 25** Mesh of quadratic hexahedral finite elements, generated on the surfaces resulting from the surface fitting

key aspects. Firstly, the movement of the cameras is restricted onto a circle, which reduces the number of parameters associated with them. Secondly, the modified bundle adjustment formulation takes distortion effect of the optical interface into account by simulating the refraction of the light rays explicitly. In the second step, the method removes outlier points from the cloud by applying the random sample consensus algorithm. This yields a set of inlier points and a best-fit cylinder on these points. The next step iteratively deforms this cylindrical surface toward the inlier points by an active surface fitting procedure, which results in a B-Spline surface, accurately representing the geometric model. In the last step, a mesh of high-order quadrilaterals is created, which are then swept along the local surface normals, yielding high-order hexahedra.

It was shown by numerical examples that the average distance of the geometric representation provided by each step lies within the range of 1% of the characteristic size of the reference geometry. In particular, considerable reduction of the error can be achieved by taking the refractive effects into account by means of the modified bundle adjustment formulation.

Further extensions of the reconstruction procedure could aim at a more effective estimation of the camera motion parameters and the refractive interface. Because the camera moves along a circular path, the method of [23] or [24] could be used for the motion estimation, instead of manual measurements. The parameters of the refractive interface might be estimated by attaching a calibration grid on them—the markers in the grid are not subject to any refractive distortion; therefore, the shape of the interface might be measured using standard techniques, as in [25,26].

**Acknowledgements** The authors thank Mr. Avihai Uzan (Department of Mechanical Engineering, Ben Gurion University, Israel) for his assistance with the experiment in Sect. 3.3. The research was funded by the German-Israeli Foundation for Scientific Research and Development under Grant No. GIF-1189-89.2/2012. This support is gratefully acknowledged.

## References

- Zhang, Y.J.: Image-Based Geometric Modeling and Mesh Generation, vol. 3. Springer, New York (2012)
- Jordt-Sedlazeck, A., Koch, R.: Refractive structure-from-motion on underwater images. In: 2013 IEEE International Conference on Computer Vision (ICCV), pp. 57–64. IEEE (2013)
- Chen, X., Yang, Y.-H.: Two-view camera housing parameters calibration for multi-layer flat refractive interface. In: Proceedings of the IEEE Conference on Computer Vision and Pattern Recognition, pp. 524–531 (2014)
- Kutulakos, K.N., Steger, E.: A theory of refractive and specular 3D shape by light-path triangulation. *Int. J. Comput. Vis.* **76**(1), 13–29 (2008)
- Qian, Y., Gong, M., Yang, Y.-H.: Stereo-based 3D reconstruction of dynamic fluid surfaces by global optimization. In: Proceedings of the IEEE Conference on Computer Vision and Pattern Recognition, pp. 1269–1278 (2017)
- Szabó, B.A., Düster, A., Rank, E.: The p-version of the finite element method. In: Stein E, de Borst R, Hughes TJR (eds) *Encyclopedia of Computational Mechanics*, chapter 5, vol. 1, pp. 119–139. Wiley (2004)
- Wong, K.H., Chang, M.M.-Y.: 3D model reconstruction by constrained bundle adjustment. In: Proceedings of the 17th International Conference on Pattern Recognition, vol. 3, pp. 902–905. IEEE (2004)
- Mulsow, C.: A flexible multi-media bundle approach. *Int. Arch. Photogramm. Remote Sens. Spat. Inf. Sci.* **38**, 472–477 (2010)
- Belden, J.: Calibration of multi-camera systems with refractive interfaces. *Exp. Fluids* **54**(2), 1463 (2013)
- Pottmann, H., Leopoldseder, S.: A concept for parametric surface fitting which avoids the parametrization problem. *Comput. Aided Geom. Des.* **20**(6), 343–362 (2003)
- Sorger, C., Frischmann, F., Kollmannsberger, S., Rank, E.: Tum.geoframe: automated high-order hexahedral mesh generation for shell-like structures. *Eng. Comput.* **30**(1), 41–56 (2014)
- Hartley, R.I., Zisserman, A.: *Multiple View Geometry in Computer Vision*, 2nd edn. Cambridge University Press, Cambridge (2004). ISBN: 0521540518
- Triggs, B., McLauchlan, P.F., Hartley, R.I., Fitzgibbon, A.W.: Bundle adjustment—a modern synthesis. In: *International workshop on vision algorithms*, pp. 298–372. Springer (1999)
- Glassner, A.S. (ed.): *An Introduction to Ray Tracing*. Academic Press Ltd., London (1989)
- Lowe, D.G.: Distinctive image features from scale-invariant keypoints. *Int. J. Comput. Vis.* **60**(2), 91–110 (2004)
- Moulon, P., Monasse, P., Marlet, R., et al.: OpenMVG: an open multiple view geometry library. <https://github.com/openMVG/openMVG>
- Fischler, M.A., Bolles, R.C.: Random sample consensus: a paradigm for model fitting with applications to image analysis and automated cartography. *Commun. ACM* **24**(6), 381–395 (1981)
- Cazals, F., Pouget, M.: Estimating differential quantities using polynomial fitting of osculating jets. *Comput. Aided Geom. Des.* **22**(2), 121–146 (2005)
- Pottmann, H., Hofer, M.: Geometry of the squared distance function to curves and surfaces. In: Hege, H.-C., Polthier, K. (eds.) *Visualization and Mathematics III*, pp. 221–242. Springer, Berlin, Heidelberg (2003)
- Bradski, G.: The OpenCV Library. *Dr. Dobbs' Journal of Software Tools* 2236121 (2000)
- Yossef, O.E.: Experimental investigation of arteries' mechanical properties: compressibility, passive and active responses. Master's thesis, Department of Mechanical Engineering, Ben-Gurion University, Israel (2017)
- Zhang, Z.: A flexible new technique for camera calibration. *IEEE Trans. Pattern Anal. Mach. Intell.* **22**(11), 1330–1334 (2000)
- Jiang, G., Tsui, H.-T., Quan, L., Zisserman, A.: Single axis geometry by fitting conics. In: *European Conference on Computer Vision*, pp. 537–550. Springer (2002)
- Kumar, P., Miklavcic, S.J.: Integrated self-calibration of single axis motion for three-dimensional reconstruction of roots. *IET Comput. Vis.* **9**(6), 850–856 (2015)
- Ke, X., Sutton, M.A., Lessner, S.M., Yost, M.: Robust stereo vision and calibration methodology for accurate three-dimensional digital image correlation measurements on submerged objects. *J. Strain Anal. Eng. Des.* **43**(8), 689–704 (2008)
- Yamashita, A., Hayashimoto, E., Kaneko, T., Kawata, Y.: 3-D measurement of objects in a cylindrical glass water tank with a laser range finder. In: *IEEE/RSJ International Conference on Intelligent Robots and Systems, 2003. (IROS 2003)*. Proceedings. 2003, vol. 2, pp. 1578–1583. IEEE (2003)

**László Kudela** studied mechatronics (B.Sc.) at the Budapest University of Technology and Economics and computational mechanics (M.Sc.) at the Technical University of Munich (TUM). He is currently a research assistant at the Chair for Computation in Engineering at TUM. His main research interests lie in image-based finite elements and geometric representation techniques for non-conforming discretization methods.

**Felix Frischmann** studied civil engineering (B.Sc.) and computational mechanics (M.Sc.) at TUM. He was a research assistant at the Chair for Computation in Engineering at TUM focusing on FEM mesh generation and smooth coupling of preprocessing tools and numerical simulation. Currently, he is involved in the companies Locis GmbH and ffr Engineering as founder and director. The focus of his professional portfolio lies in the field of CAD, CAM, and CAE software development and product model preprocessing for numerical simulations.

**Ofry E. Yossef** received his Bachelor and Master degree from the mechanical engineering department of Ben-Gurion University, Beer-Sheva, Israel. His master degree in experimental biomechanics focused on the mechanical properties of arteries. He is currently working at an R&D private company based in Holon, Israel.

**Stefan Kollmannsberger** is a senior researcher at the Technical University of Munich. He leads the research group Simulation in Applied Mechanics at the Chair for Computation in Engineering. His research interests evolve around the integration of geometric modeling and computational mechanics in both academia and practice and the development of highly accurate yet fast numerical methods.

**Zohar Yosibash** is a professor of mechanical engineering at the Tel Aviv University, Israel, where he is the Head of the Computational Mechanics and Experimental Biomechanics Laboratories. He received his B.Sc. in Aeronautical Engineering in 1987 from the Technion, Israel, Institute of Technology, his M.Sc. in Applied Mathematics in 1991 from Tel-Aviv University, and his D.Sc. in Mechanical Engineering in 1994 from Washington University in St. Louis, USA. During 2002–2007, he held a visiting associate professorship at the division of applied Mathematics at Brown University.

**Ernst Rank** is the head of the Chair for Computation in Engineering at the Technical University of Munich, Germany. He studied mathematics and physics at the Ludwig-Maximilians-Universität München and obtained his doctoral degree from the Faculty for Civil Engineering and Geodesy of the Technical University of Munich in 1985. He became a DAAD fellow at the University of Maryland, College Park, USA, until 1986. From 1987 to 1990, he held the position of senior scientist at the Corporate Research and Technology Department of SIEMENS AG in Munich. He was appointed professor for Numerical Methods and Information Science in Civil Engineering at the University of Dortmund in 1990 and has held the chair for Computation in Engineering at the Technical University of Munich since 1997. Prof. Rank held the office of First Vice President of TUM from 2002 to 2008. In April 2015, Prof. Rank was appointed Director of the TUM Institute for Advanced Study (TUM-IAS). His main areas of research are in Computational Engineering and the modeling of products and processes in civil engineering.